Search for the Excited States of Neutron-Rich Krypton Isotopes

by

Sebastien Roy-Garand

A THESIS SUBMITTED IN PARTIAL FULFILMENT OF
THE REQUIREMENTS FOR THE DEGREE OF

BACHELOR OF SCIENCE

in

Honours Physics

(Department of Astronomy and Physics, Dr. Rituparna Kanungo supervising faculty)

.....

.....

.....

.....

.....

SAINT MARY'S UNIVERSITY

June 2, 2020

Abstract

Search for the Excited States of Neutron-Rich Krypton Isotopes

by *Sebastien Roy-Garand*

submitted on June 2, 2020:

The complex nature of nuclear structure is governed by strongly interacting nucleons. As described by the nuclear Shell Model, the building blocks of atomic nuclei, protons and neutrons, arrange themselves in discrete quantized orbitals that group into shells. These shells are considered closed when the number of protons or neutrons equate to the magic nucleon numbers. In neutron-rich nuclei which are created via the r-process in nature's neutron-rich environments, expectedly, potential changes in shell structure and magic numbers is discussed theoretically. Identifying shell closures in neutron-rich isotopes would help constrain theoretical models for r-process nucleosynthesis. Krypton isotopes are of interest as current experimental evidence points towards changes in shell structure taking place in the neutron-rich region of N=50-60. Following the trend of the neighbouring elements, Sr and Zr, there is potential of shape coexistence manifesting in these Kr isotopes. Such a discovery will help provide further information on the nuclear force which governs the evolution of nuclear structure. Therefore, the excited states of select Kr nuclei were investigated to provide further data on the shell structure of neutron-rich isotopes. To investigate this neutron-rich region, a beam of ^{93}Kr was received at the IRIS reaction spectroscopy

station located at TRIUMF. Through the use of a solid deuterium target, both the reaction channels ^{93}Kr(d,d)^{93}Kr and ^{93}Kr(d,p)^{94}Kr were investigated.

Contents

List of Figures

Chapter 1

Introduction

1.1 Rare-Isotopes and Neutron-Rich Nuclei

Everything we encounter in our day-to-day lives is composed of atoms, from the air we breathe to the organisms around us. All of which can be broken down into protons and neutrons composing a nucleus which is surrounded by electrons. But how did this all come to be? How could the hundreds of species of atoms we interact with be formed from three simple building blocks? There are two ingredients needed to synthesize the elements in our universe, matter and energy, which is largely why the formation of nearly all elements up to iron can be attributed to nuclear fusion in stars. Elements beyond iron rely on violent mechanisms which introduce an abundance of energy and neutrons for their nucleosynthesis such as supernovae and neutron-star mergers.

In such environments, neutron capture and beta decay mechanisms manifest forging the majority of heavy elements we see on earth. The underlying truth to this number is that in reality, there are thousands of species of nuclei which can form. Some nuclei may not have been present in the stardust which formed our solar system but in the case of some others, although they may have once been present, they no longer are.

As mentioned earlier, nuclei are an arrangement protons and neutrons. For any nucleus, the number of protons determines the element, but one element may come in a variety of species depending on the number of neutrons. All variants of an element with different neutron numbers are known as isotopes. Only a small fraction of the isotopes in the universe are stable, meaning that the remaining majority have a lifespan specified by their half-life. These non-stable isotopes are known as rare-isotopes. Even the production mechanisms in charge of element synthesis do not understand their own boundaries as they continue to add nucleon after nucleon pushing farther into the realm of unbalanced proton to neutron ratio. The eventual fate of all rare-isotopes is that they will someday become a different, but stable, isotope through a chain of decays. In nuclear physics, it is key to understand the properties of these rare-isotopes as this information will help further our knowledge of the nuclear force which governs nuclear structure and the formation of isotopes.

In this thesis there is a special subset of rare-isotopes known as neutron-rich isotopes which were of interest. These are isotopes within which the number of neutrons far outweighs the number of protons in the nucleus. In this neutron-rich region, the theoretical models built on descriptions of stable nuclei breaks down. The goal of studying neutron-rich nuclei is to better understand the r-process, one of the production mechanisms for heavy isotopes and more specifically, to find the unknown features of neutron-rich isotopes that will give us a more complete understanding of the nuclear force and help guide nuclear models.

1.2 Nuclear Shell Model

Much to the likes of electrons, nucleons arrange themselves into orbitals which characterise the nuclear structure. The potential within which the nucleons sit is governed by the strong interaction between nucleons. While this is complex and not exactly expressed in an analytical form, the average potential can be described by some phenomenological functional forms. One such form is the Woods-Saxon potential,

$$V(r) = \frac{-V_0}{1 + exp[\frac{r-R}{a}]} \tag{1.1}$$

This potential is described by the mean radius (R) of the nucleus and the diffuseness of the potential (a). The energy levels are filled in accordance to the Pauli exclusion principle, separately for protons and neutrons as they are non-identical particles. With the inclusion of a spin-orbit coupling term, large gaps are found between energy levels at proton or neutron number equivalent to 2, 8, 20, 28, 50, 82 and 126 signifying shell closures [1].

The process of deriving these numbers, known as magic numbers, is shown in Figure 1.1. First, the energy of each quantum state of the system is attained from the potential in equation (1.1). In addition, the spin-orbit interaction causes all non-spherically symmetric levels to be split into two levels with angular momenta $j = l \pm 1/2$, where l is the orbital angular momentum quantum number and j is the total angular momentum. Each energy level then has a degeneracy of $2j + 1$. The resulting sum of the occupancy of each energy level up to a shell closure is where the magic numbers arise as shown in red (Fig. 1.1).

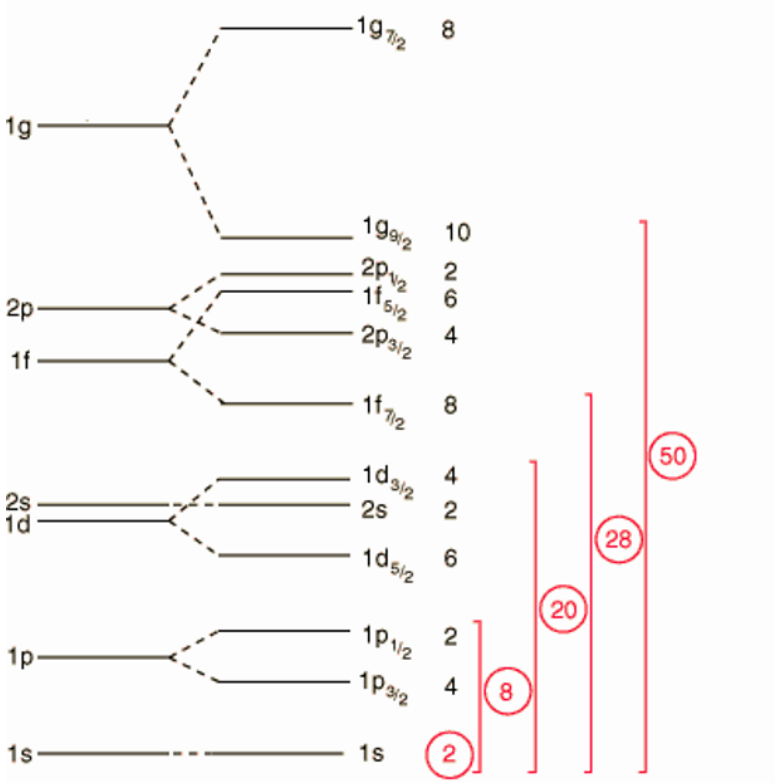

Figure 1.1: Identification of the magic numbers from nuclear energy levels.[2]

Experimentally, the magic numbers were first identified by Maria Goeppert Mayer in the year 1949 when she recognized that there was an abundance of elements at specific proton (Z) and neutron (N) numbers. Namely, Z=50 and 82 and N=50, 82 and 126. In distinguishing specific isotopes with neutron or proton number corresponding to those listed above, she noted that they were largely stable or long-lived compared to their neighbours [3].

With the understanding that magic numbers play a large role in the stability of isotopes, it can be concluded that there is a bias imposed on the processes' of nucleosynthesis due to this fact. The abundance of isotopes tends to be concentrated around the magic numbers since a significant amount of energy is required to then begin a new shell. This is the case for the r-process which is the dominant production

mechanism of neutron-rich nuclei. Also in this region, other effects begin to dominate which leads to the break down of the traditional formulation of the shell model with the rise of new unpredicted shell closures. For this reason, experimental data for neutron-rich isotopes is of key importance in assisting theoretical models of the r-process.

1.3 Shell Evolution in the N=50-60 Region

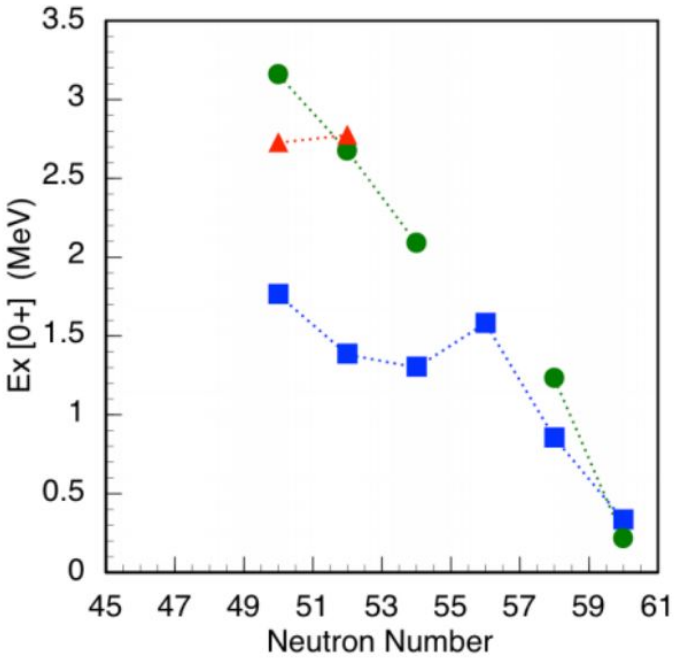

Figure 1.2: Excitation energy comparison of the first 0^+ excited states of Krypton(red), Strontium(Green) and Zirconium(Blue) isotopes from N=50-60.[4]

One such region where this change in shell structure is suspected to take place is the N=50-60 range of neutron-rich nuclei. Due to the asymmetry in proton and neutron number, the nuclear forces between closed shells may affect single particle orbits. The positioning and ordering of these single particle energy levels is what governs

excited states, thus excited states themselves can give insight into changes in shell structure. For the region of interest, N=50-60, the second 0^+ state can be used to understand such a phenomena. In Figure 1.2, Sr(Z=40) and Zr(Z=38) demonstrate a decreasing trend afterwards of the expected shell closure at magic number N=50. As seen in this figure, Kr(Z=36) does not demonstrate this decreasing trend as there is an increase in the energy of the 0_2^+ excited state from N=50 to N=52. For this reason, experimental information is required to assess the evolution of the 0_2^+ excited state for Kr isotopes beyond N=52.

For ^{94}Kr(N=58), the theoretical predictions of the 0_2^+ state are widely varying. A study by Rodríguez[5], using a proton-neutron interacting boson model (IBM-2) Hamiltonian, predicted an excitation energy of ∼700 keV for the 0_2^+ state. A different study conducted by Albers et al.[6] which utilized the symmetry-conserving configuration-mixing (SCCM) method predicts this state to be located at ∼3 MeV. By observing the 0_2^+ state in ^{94}Kr, further insight would be granted into the mechanism causing this evolution in shell structure.

1.4 Nuclear Shape and Shape Coexistence

The idea of nuclear shapes was introduced as early as 1937 from the works of Bohr and Kalcker[7]. At this point, the interplay of shape and nuclear structure was yet to be understood. These shapes produced by the nucleus are a result of the nuclear quadrupole moment (Q), which describes the charge distribution of the nucleus. If $Q = 0$, the nucleus will be spherically symmetric. The nucleus will be prolate if $Q > 0$

and oblate if $Q < 0$ [1]. In general, a nucleus is spherical at closed shells, oblate when near a closed shell and prolate between shells [8].

In the year 1956, the phenomenon of shape coexistence was first discovered by observation of the 0^+ states in ^{16}O [9]. This discovery opened up a new research area in nuclear physics which looks to investigate and understand shape coexistence. In Ref.[10], shape coexistence is described as the "interplay of two opposing tendencies": firstly, there is the effect coming from closed shells leading to a spherically symmetric nucleus and secondly, there is the residual interactions between protons and neutrons leading to a deformed nucleus. Through both of these effects, a mixing will occur across states with identical angular momentum values.

For even-even nuclei, shape coexistence is manifested in close by low lying 0^+ states. The first of which being the ground state and the second of which having a reduced energy due to the aforementioned residual interactions between protons and neutrons. For ^{94}Kr, the predicted energy of 700 keV in Ref.[5] for the 0_2^+ excited state makes it probable that shape coexistence is manifesting in this neutron-rich region of Kr isotopes. On the other hand, predicted high excitation energy in Ref.[6] could point to a lack of shape coexistence.

1.5 Nuclear Reactions

The use of nuclear reactions to investigate properties of atomic nuclei has been employed for nearly a century. The first designed experiment to study the nucleus via nuclear reactions was the renowned gold foil experiment conducted by Rutherford

using an alpha source for scattering experiments. In the modern day, experimental research in nuclear physics is largely dependent on large facilities capable of performing various types of nuclear reactions and at different energies.

The general concept for the studied reactions of this experiment, performed in inverse kinematics, is that a beam of heavy particles (A) is impinged on a target of light particles (b) from which results an outgoing heavy product (C) and light product (d).

$$A + b \longrightarrow C + d \tag{1.2}$$

Such a reaction is written in short form as $A(b, d)C$. There are two types of reactions of interest which took this form: scattering reactions and transfer reactions.

In the case of a scattering reaction, the identity of the colliding nuclei are preserved. Meaning that,

$$A + b \longrightarrow A + b \tag{1.3}$$

With sufficient incoming particle energy, the reaction resembles a relativistic collision between the two nuclei. The reaction shown in (1.3) is a special case known as elastic scattering where the kinetic energy is conserved through the reaction.

It is also a possibility during a scattering reaction that nucleus A may go into an excited state resulting in the kinetic energy not being conserved. This reaction, known as inelastic scattering is as follows.

$$A + b \longrightarrow A^* + b \tag{1.4}$$

Such a reaction allows for the excited states of nucleus A to be explore as the energy of the ejectile b then relates to the state at which A was excited into.

The second reaction of interest is a transfer reaction. In this reaction, a nucleon (or a group of nucleons) is either transferred to or transferred from the target nucleus to the beam nucleus. Thus, the identities of the colliding nuclei are not preserved, hence the reaction form resembling (1.2). Once again, in this reaction, C may be formed into an excited state, in which case d will have an energy relating to the state at which C was excited into.

Chapter 2

Description of Experiment

This experiment was performed at TRIUMF, Canada's national particle accelerator centre, located in Vancouver, BC. At TRIUMF, there are a number of research facilities whose exploration into rare-isotopes is at the forefront of subatomic physics. This research is enabled by TRIUMF's cyclotron, the largest of its kind in the world. This cyclotron is capable of accelerating a beam of protons up to 500 MeV which in turn produces the radioactive beam for experimentation. The ability to produce rare-isotopes is extremely challenging and is therefore invaluable as most of the isotopes of interest, which naturally occur in extreme environments, are very short lived.

2.1 Radioactive Ion Beam Production at TRIUMF

The radioactive isotope beam (RIB) production method utilized at TRIUMF is known as, isotope seperation on-line (ISOL). In ISOL facilities, a primary beam of particles is impinged onto a target. This beam causes fragmentation and fission processes' within the target which produces a variety of radioactive nuclei. Due to the nature of this process, the ability to separate out the isotope of interest is necessary. This is managed by a mass separator which differentiate isotopes by their

mass-to-charge ratio.

In regards to this experiment, a beam of 500 MeV protons were impinged onto a uranium carbide target. From the resulting array of isotopes, ^{93}Kr was extracted with a mass separator. Following, the RIB was re-accelerated to $\sim 8A$ MeV and sent to the ISAC rare-isotope reaction spectroscopy station (IRIS) [11] for performing the experiment.

2.2 IRIS Experimental Setup

IRIS is a research facility at TRIUMF located in the ISAC-II experimental hall. With the unique feature of housing a solid D_2/H_2 target, the elastic, inelastic and transfer reactions are studied in inverse kinematics. The main components of IRIS, shown in Figure 2.1, are the Ionization Chamber (IC), the solid D_2/H_2 target and the charged particle detectors, including both silicon detectors and a scintillator [11].

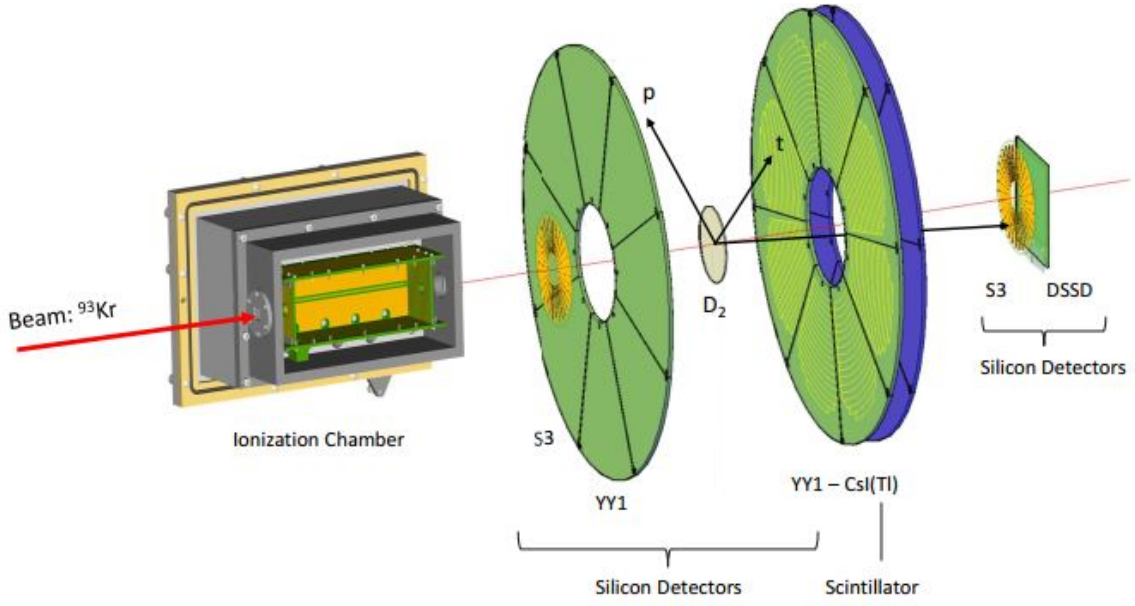

Figure 2.1: IRIS experimental setup schematic. (adopted from [12])

2.2.1 Ionization Chamber

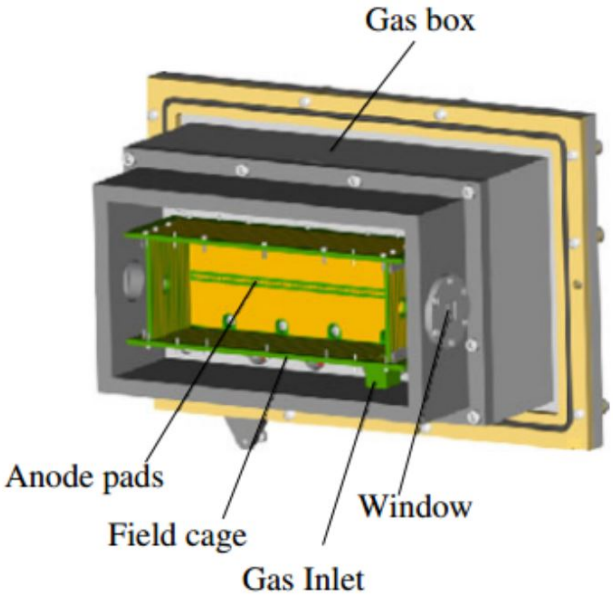

Figure 2.2: Ionization Chamber schematic. (adopted from [11])

The Ionization Chamber (IC) is used in the IRIS experimental setup for identifying beam contaminants. The IC, located upstream from the other components, is filled with isobutane gas ($HC(CH_3)_3$) at a pressure of 19.5 Torr. After the beam passes through a 50 nm window of Si_3N_4, it then travels through the gas where each species within the beam deposits energy by ionization. Within the gas box is a field cage which is negatively charged, creating an electric field which directs the electrons produced by ionization towards the anode pads. The collected charge sends a voltage signal from the anode pads to the data acquisition system (DAQ). The beam then exits through a second Si_3N_4 window of 50 nm in thickness and proceeds into the scattering chamber.

2.2.2 D_2/H_2 Target

The unique feature of IRIS is the thin windowless D_2/H_2 target. As IRIS aims to measure reactions of rare-isotopes located far from stable nuclei with a beam of relatively low intensity, this target is of paramount importance due to its very high density which maximizes the number of interactions.

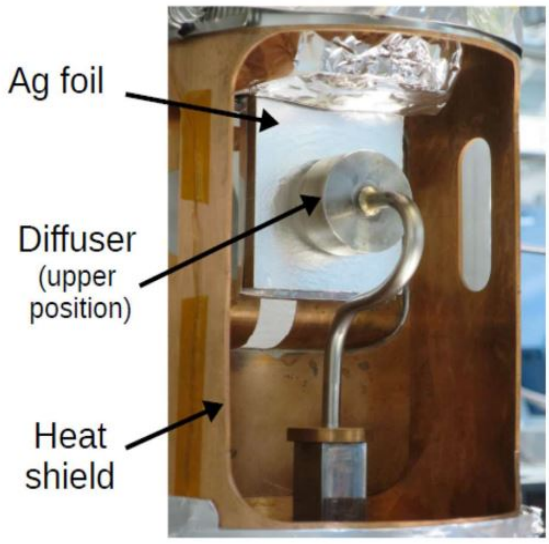

Figure 2.3: Solid D_2/H_2 target schematic. (adopted from [12])

As shown in Figure 2.3, the target module is composed of a heat shield, diffuser and Ag foil. The 4.6 μm thick Ag foil is mounted onto a copper cell with a 5 mm diameter hole to allow for the passage of the beam. This copper cell is then cooled by a helium cryocooler with a helium compressor to $\sim$4 K and the outer heat shield reaches a temperature of $\sim$24-27 K in effort to minimize the radiative heat loss. The diffuser which sources the D_2/H_2 gas is positioned on an actuator which moves it into and out of the beam path. To form a target once the Ag foil is cooled, the diffuser is placed in the upper position as displayed in Figure 2.3 and the D_2/H_2 gas is sprayed

onto the foil. This process produces a target of ∼50-100 μm in thickness.

For the beam delivery of this experiment, it is nescessary to note that the target module was positioned such that the Ag foil is facing upstream. This means that any light particle resulting from forward angle reactions ($\theta_{Lab} < 90°$) will first pass through the Ag foil, losing energy, prior to detection.

2.2.3 Charged Particle Detectors

For the detection of charged particles, IRIS is equipped with arrays of silicon detectors as well as a scintillator which can be seen in Figure 2.1. For measureing reactions emitting particles which are also in the backward angle, namely the ^{93}Kr(d,p)^{94}Kr reaction for $\theta_{Lab} > 90°$, there are two sillicon detectors, referred to as YY1 and S3d1. In the forward angle direction ($\theta_{Lab} < 90°$) where the reactions ^{93}Kr(d,p)^{94}Kr, ^{93}Kr(d,d)^{93}Kr and ^{93}Kr(d,t)^{92}Kr are detected, there is a silicon detector, YY1, and a scintillator, CsI(Tl), placed immediately behind it to form a detector telescope. In both cases, whether the light particle is going in the forward or backward angle direction, the massive beam particle retains its forward momentum allowing it to be detected in a double sided silicon strip detector (DSSD) placed further downstream at zero degrees.

The YY1 detector is a silicon strip detector array which has 8 azimuthal segments (one of which is in Fig. 2.4). Each sector is subdivided into 16 radial rings resulting in a total of 128 detector channels for the array. Each channel consists of an electrically biased silicon strip which records the energy deposited from charged particle

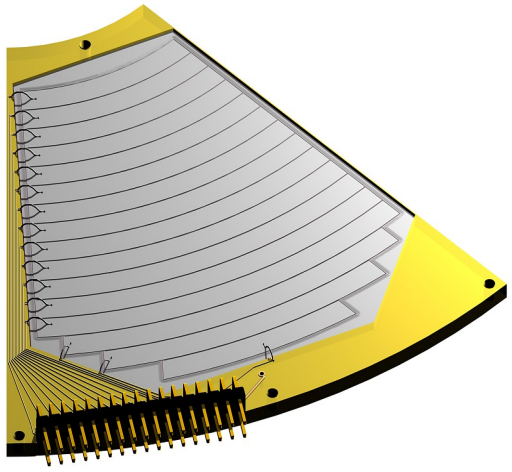

Figure 2.4: YY1 detector segment. (adopted from Ref.[13])

interactions. Having the ring segmentation allows to have an angular value (θ_{Lab}) associated to the incident light particle. Due to the nature of these rings having a discrete width, θ_{Lab} is recorded as the average angle of the strip. To account for this, the recorded value of θ_{Lab} is randomized between the angle at the top of the strip and the angle at the bottom of the strip during analysis.

In the low energy regime of reaction products, which is the case for backward angle reactions, the strips will detect the total energy of the light particle. In the higher energy regime the strips will only record energy loss by the light particle making it necessary to couple the YY1 in the forward angle direction with a scintillator. The scintillator as a whole is composed of 16 CsI crystals with a Tl dopant for increased light emission efficiency. As the CsI(Tl) detector is coupled with the downstream YY1 detector, which is displayed in Figure 2.1, the crystals are placed such that two azimuthal segments are positioned behind each of YY1 azimuthal segments. There are two benefits resulting from coupling of these two detectors. First, as mentioned

earlier, the YY1 silicon detector is unable to stop high energy light particles, thus, after these particles lose energy through the YY1, the remaining energy will be deposit into the CsI(Tl). This allows for particle identification by ΔE-E (see Section 3.3). Secondly, on it's own, the CsI(Tl) detector is incapable of determining angle, but with the YY1 detector having the capability of assigning angle to particle counts due to the ring segmentation, all counts in the CsI(Tl) detector which are in coincidence with the YY1 detector will share this angular value. This is of key importance for the generation of a Q-value spectrum (see Section 3.4.1).

Further downstream is the DSSD detector. This silicon detector has 16 strips on the front and back spanning in the horizontal and vertical direction. It is positioned directly along the beam axis and is used to detect the total remaining energy of the beam particles. In doing so, the DSSD renders the ability for the target thickness to be measured as described in Section 3.2.2.

Chapter 3

Data Analysis

In the following sections the steps taken to render a physical interpretation from the raw data will be described. Prior to the analysis of individual reaction channels, general properties of the RIB must be resolved. This involves determining the beam energy as well as identifying ^{93}Kr within the beam. This in turn will allow for target thickness to be determined. Once the detectors are calibrated, individual reaction channels may then be selected for further analysis.

3.1 Incident Beam Identification

As mentioned in Section 2.1, impurities within the beam are expected. To identify the various species in the RIB and to isolate the isotope of interest, ^{93}Kr, the energy loss within the IC is measured. The stopping power of a charged particle passing through matter, which is the energy loss (dE) per unit length (dx), is mathematically defined as follows,

$$-\frac{dE}{dx} \propto \frac{Z^2}{v^2} \tag{3.1}$$

where Z is the atomic number and v is the velocity of the charged particle. This allows for differentiation of elements with different 'Z' within the beam. From left to right in Figure 3.1, the four peaks seen in the IC spectrum are ^{68}Zn, ^{93}Kr, ^{93}Nb

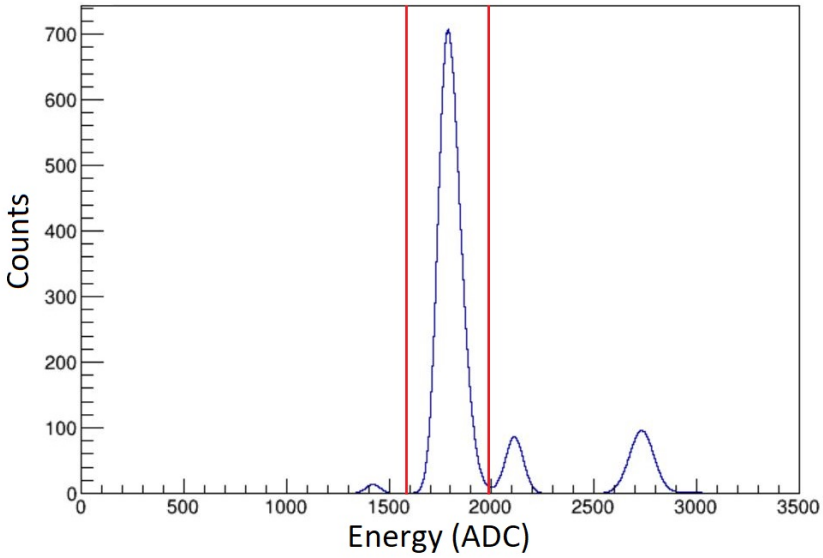

Figure 3.1: ADC spectrum of the Ionization Chamber with red gate placed around ^{93}Kr peak

and ^{118}Sn. To select only the events corresponding to ^{93}Kr, a gate is place around the krypton peak. This is represented by the red vertical lines in Figure 3.1. Moving forward with the analysis using this condition will constrain the data in the scattering chamber to only particle hits originating from a beam particle within this gate.

3.2 Detector Calibrations

In this section the calibration of the YY1 and CsI(Tl) detectors will be discussed. The energy values of the raw data are recorded in ADC channel number. ADC stands for analog to digital converter where in the case of IRIS, an analog signal is received from the detectors which is then digitized and classified by peak voltage into one of 4096 channels. This ADC channel value must then be converted to a physical energy

value, MeV. The equation for this conversion from ADC to MeV is,

$$E = g \times (c - p) \tag{3.2}$$

$$g = \frac{E}{(c - p)} \tag{3.3}$$

where E is the energy in MeV, g is the gain (i.e. scaling factor from ADC to MeV), c is the ADC channel number corresponding to the peak of the observed pulse height spectrum and p is the pedestal which represents the zero point of the detector channel. Equation (3.2) shows the conversion from ADC to energy which can be rearranged in the form of equation (3.3) for the purpose of calibration. This calibration is conducted with a source of known energy value meaning that the calibration within a small energy range is extrapolated to the full energy range of the detector. For this reason, lower energy detectors such as the YY1's were calibrated using a triple-alpha source of ∼5 MeV and the CsI(Tl) detector, which detects the total energy of the light particles, was calibrated with elastic scattering of the ^{93}Kr beam. In doing so the error resulting from extrapolation is minimized.

3.2.1 YY1 Detectors

For the calibration of the YY1 detectors, a triple alpha source of ^{241}Am, ^{244}Cm and ^{239}Pu with energies of 5.15 MeV, 5.48 MeV and 5.80 MeV was used. The alpha particles emitted from this source deposit their total energy in the YY1 channels. Figure 3.2 is the uncalibrated energy of the alpha source in all of the 128 detector

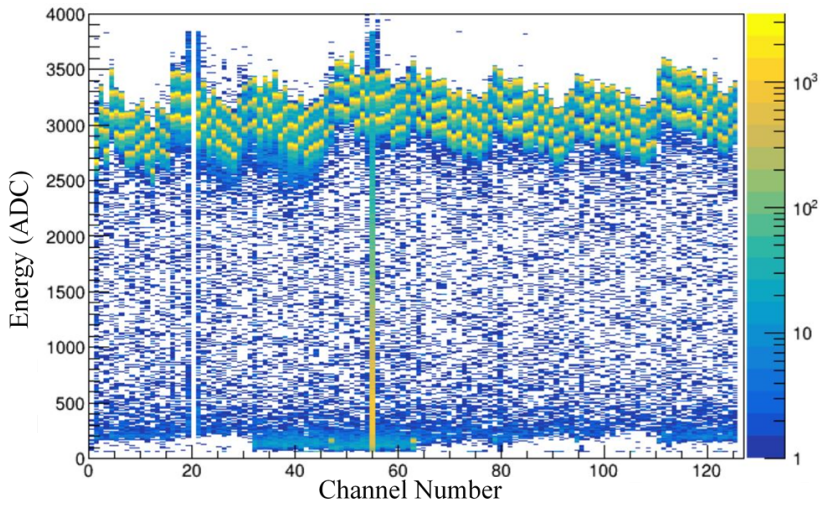

Figure 3.2: Uncalibrated YY1 alpha source spectrum

channels and Figure 3.3 is the projection of a single channel where the three alpha peaks can be seen. To calibrate a single channel, each of three peaks is fit with a Gaussian and the mean value is recorded. Following, the the mean values of the peaks are plotted against the known alpha energies and fit using a linear regression as seen in Figure 3.4. The resulting slope of this fit is the gain factor in equation (3.2) for the corresponding YY1 channel. These steps were repeated for each of the YY1 channels in order to calibrate the entire detector which gives the resulting spectrum in Figure 3.5.

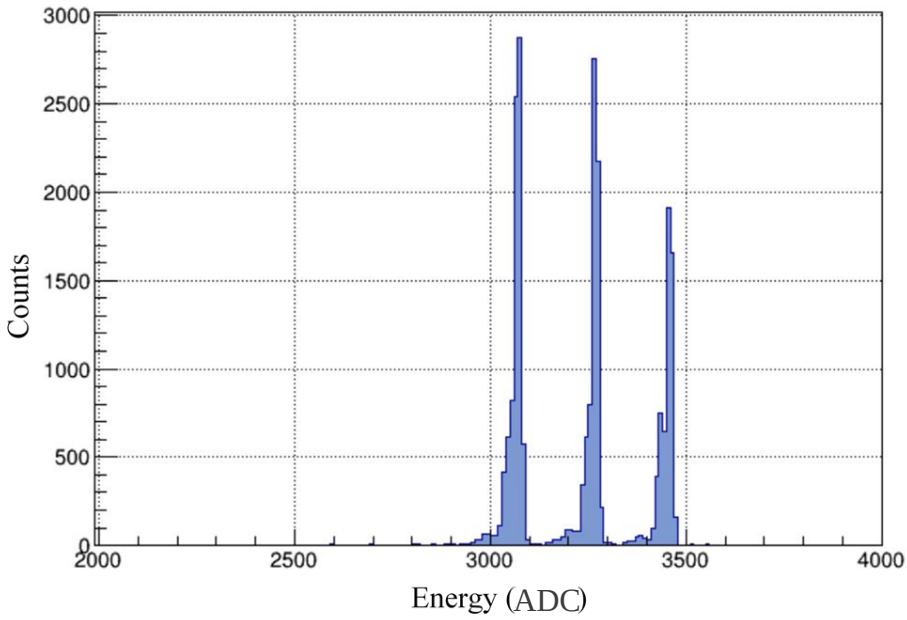

Figure 3.3: Uncalibrated alpha peaks in single YY1 channel

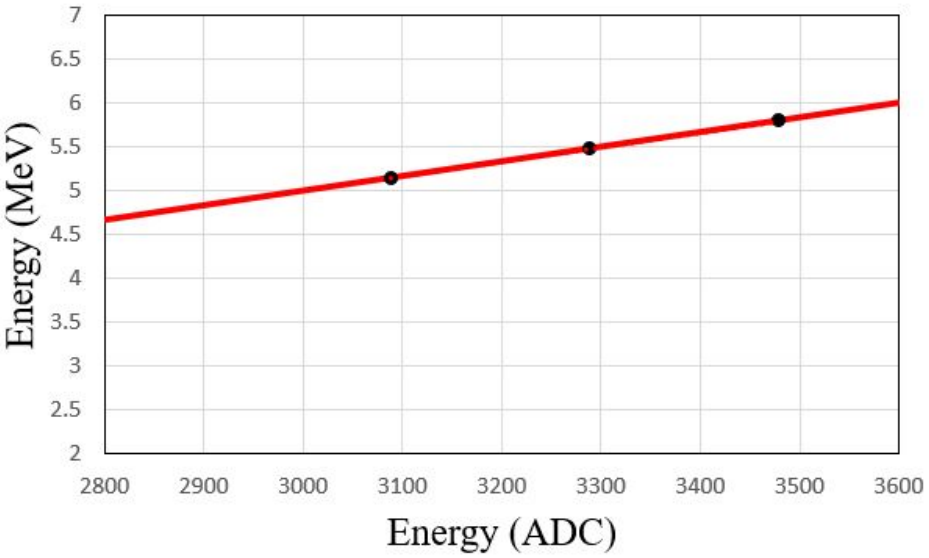

Figure 3.4: Linear regression of uncalibrated alpha energies

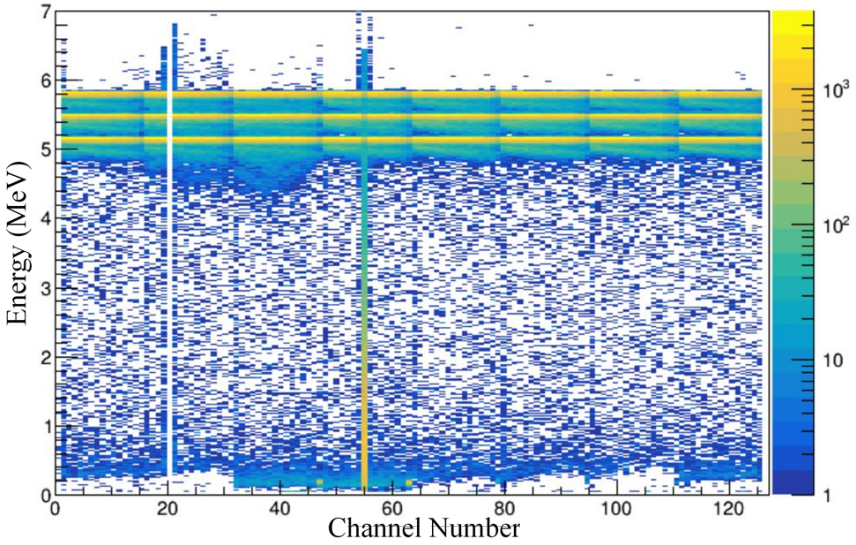

Figure 3.5: Calibrated YY1 alpha source spectrum

3.2.2 Beam Energy and D_2 Target Thickness

As the CsI(Tl) detector requires to be calibrated with the elastic scattering peak of ^{93}Kr, the beam energy and target thickness must first be resolved to determine the energy value of the light particle which is deposited in the CsI(Tl) detector.

The initial beam energy delivered was at an energy of $8.11A$ MeV. Looking at the zero degree DSSD detector energy (Figure 3.6) there was unexpected variation in the remaining beam energy. During the experiment, there was a D_2 target through data runs 5522-5601 and data runs 5619-5683. This can be seen in Figure 3.6 where the energy deposited in the DSSD is in the range on 500-530 MeV. Over the course of each target, the energy detected by the DSSD is decreasing. This would appear to suggest that the target thickness is increasing over time which very unlikely as the target is actually expected to be evaporating over time and cannot accumulate additional D_2. Therefore there are two potential causes to this shift in energy, either

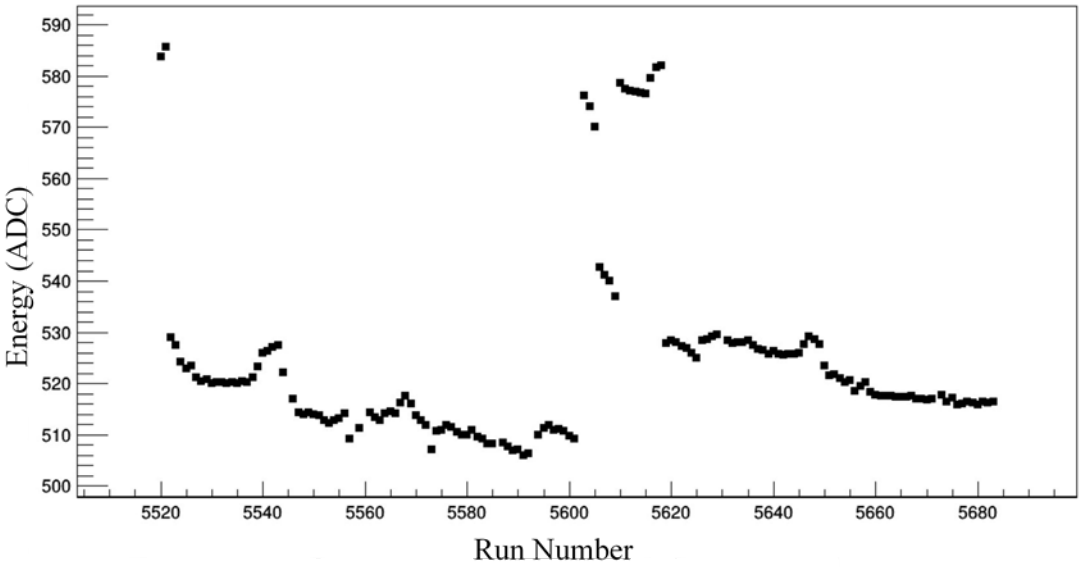

Figure 3.6: Energy measured in the DSSD detector for different data runs

the gain of the DSSD is drifting over time, or the beam energy itself is changing. By looking at the beam energy deposited in the IC as shown in Figure 3.7, there appears to be some oscillation but this is a result of the Day/Night cycle and slight changes in temperature within the Ionization Chamber. Further, there appears to be a shift upwards in energy afterwards of data run 5600 which corresponds to a decrease in beam energy. Since there was no obvious increasing or decreasing trend in Figure 3.7, but instead a jump in energy, it can be concluded that a gain drift is what is causing the unexpected decreasing energy within the DSSD. To determine the beam energy afterwards of data run 5600, the energy was retrieved from a beam energy reading which was conducted afterwards of data run 5683. Thus, data runs 5520-5600 had a beam energy of $8.11A$ MeV and data runs 5601 onwards had a beam energy of $8.01A$ MeV.

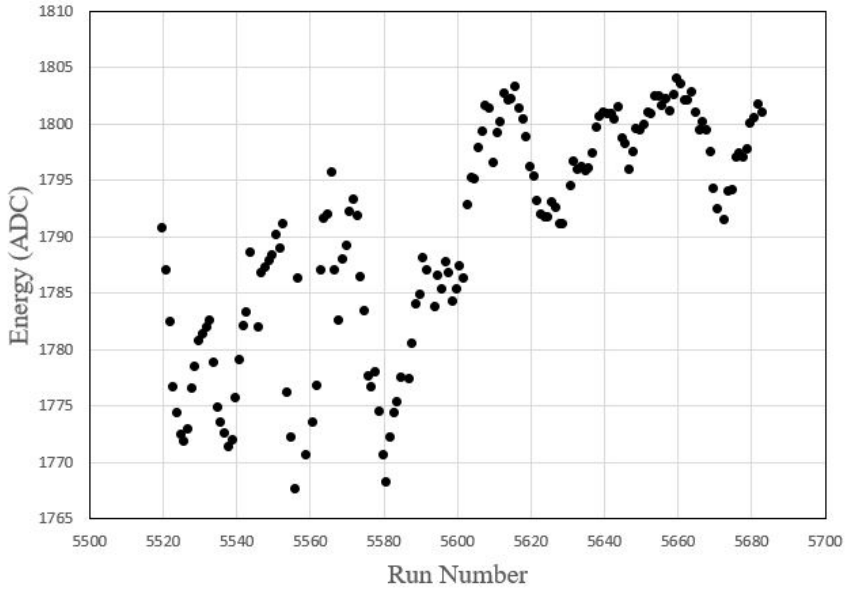

Figure 3.7: Energy deposited in the Ionization Chamber for different data runs

With the beam energy determined, the target thickness could then be determined. This is done by considering the beam energy deposited in the DSSD after the target and comparing to the beam energy deposited in the DSSD with no target formed. The difference in energy between the two can be attributed to the energy loss within the target (refer to Fig. 3.8). To extract a target thickness, the energy of the beam must be reconstructed to the point just before the silver foil for the case with and without target. This is done in the following manner,

$$E_i = E_{DSSD} + dE_{DSSDdeadlayer} + dE_{Ag} \tag{3.4}$$

where E_{DSSD} is the total energy deposited in the DSSD detector. This is then used, along with energy loss tables of ^{93}Kr in the given material, to reconstruct the beam energy with equation (3.4). The reconstructed beam energy just prior to the Ag foil for data without D_2 target (E_i) is identical to the beam energy just before the D_2

target for data with target. Thus, if E_i is the reconstructed beam energy just before the D_2 target using data without target and E_f is the reconstructed beam energy just after the D_2 target using data with target, the D_2 target thickness can be calculated with the following equation,

$$dx = \int_{E_i}^{E_f} \frac{1}{S(E)} dE \tag{3.5}$$

where dx is the target thickness and S(E) is the stopping power of the beam in solid D_2.

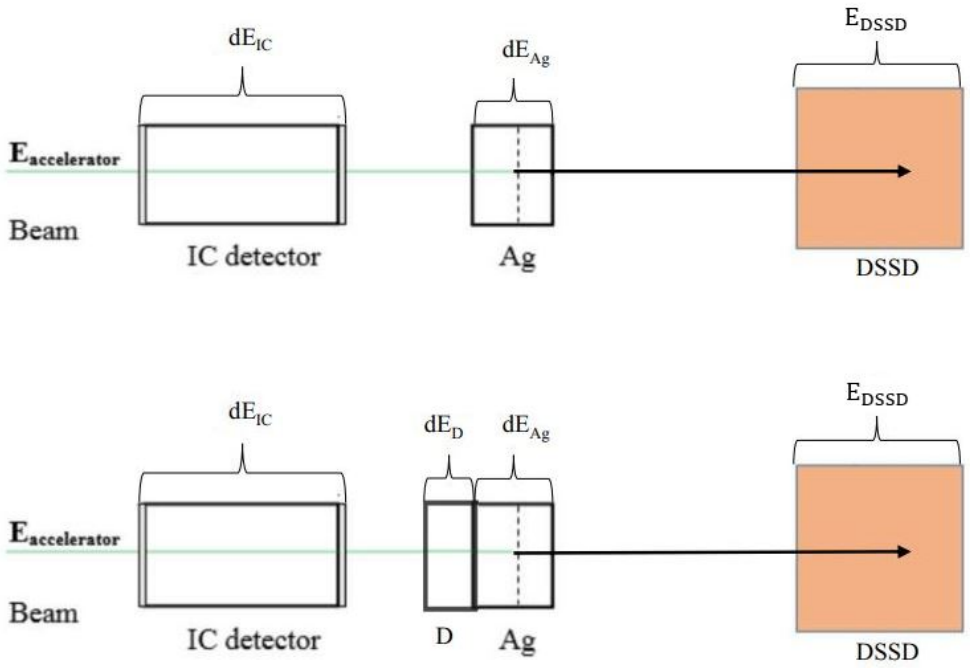

Figure 3.8: Method of determining target thickness

Usually, the target thickness is determined for each data run but as mentioned prior, there was variation in the DSSD detector gain which would not allow for this. Another big question also was, which of the DSSD energy values could be trusted? Since this gain drift appears to be occurring over time, it was concluded that the best option was to calibrate the DSSD to the known beam energy when there was

no target, then compare this energy deposited in the DSSD to the energy just after target formation in the following data run. By only comparing these two energies which are close in time, this would minimize the effects of the gain drift. For the first target, E_{DSSD} from data run 5521 (no target) used along with E_{DSSD} from data run 5522 (with target) with equation (3.4) to get a thickness of 55±3 μm. For the second target, E_{DSSD} from data run 5618 (no target) was used along with E_{DSSD} from data run 5619 (with target) to determine a target thickness of 52±3 μm. The uncertainty for the target thickness being ∼5% which accounts for the spread of the Gaussian peak of the beam energy deposited in the DSSD.

Overall, the finalized parameters for this experiment were determine to be a beam energy of 8.11A MeV with target thickness of 55±3 μm for the data runs during the first target and a beam energy of 8.01A MeV with target thickness of 52±3 μm for the data runs during the second target.

3.2.3 CsI(Tl) Calibration

As described in Section 2.2.3, the CsI(Tl) detector has a total of 16 channels, each of which must be calibrated with a gain value derived from equation (3.3). From the coupling of CsI(Tl) detector with the YY1 detector and the ability to associate angles with counts in the CsI(Tl) detector, gain values can also be found for the different angular regions corresponding to the rings of the YY1 detector. To find these gain values, elastic scattering of the ^{93}Kr beam was considered. Due to a significantly low incoming beam rate and deuteron count in the CsI(Tl) detector, each detector

channel could not be calibrated individually. Instead, each of the 16 sectors of the CsI(Tl) detectors had to be calibrated as a whole with no angular consideration.

As with all calibrations, well defined energy values are used as reference. For the calibration of the CsI(Tl), the elastic ^{93}Kr(d,d)^{93}Kr reaction was simulate to compare with experimental data. In this simulation, the beam of ^{93}Kr was given the beam energy determined in Section 3.2.2. This beam then loses energy through the first window of the Ionization Chamber, the isobutane gas, and then the second window of the Ionization Chamber. Following is the D_2 target where the scattering interaction can occur randomly at any point within the target. So, on average it is considered that the interaction point is at the center, i.e. at half-target thickness. The scattered light particle then looses energy as it exits the target at a given angle. Energy is further lost by the light particle traveling at angle θ_{Lab} as it passes through the Ag foil, the YY1 detector and the mylar cover of the CsI(Tl) crystal. The remaining energy is then considered to be detected by the CsI(Tl) detector. The resulting simulated energy of the ^{93}Kr(d,d)^{93}Kr reaction can be seen in Figure 3.9.

To match the conditions of the simulation, corresponding conditions had to be placed on the experimental data. First, the ^{93}Kr peak was gated on in the IC. Second, the ^{93}Kr(d,d)^{93}Kr reaction was gated on in the YY1-CsI(Tl) particle identification plot as shown in Figure 3.10 (see Section 3.3 for further information on particle identification). Finally, since only the ground state is being considered, the ground state locus had to be gated on in the kinematic plot of CsI(Tl) energy as shown in Figure 3.11.

With both the simulated and experimental data ready, the calibration could then

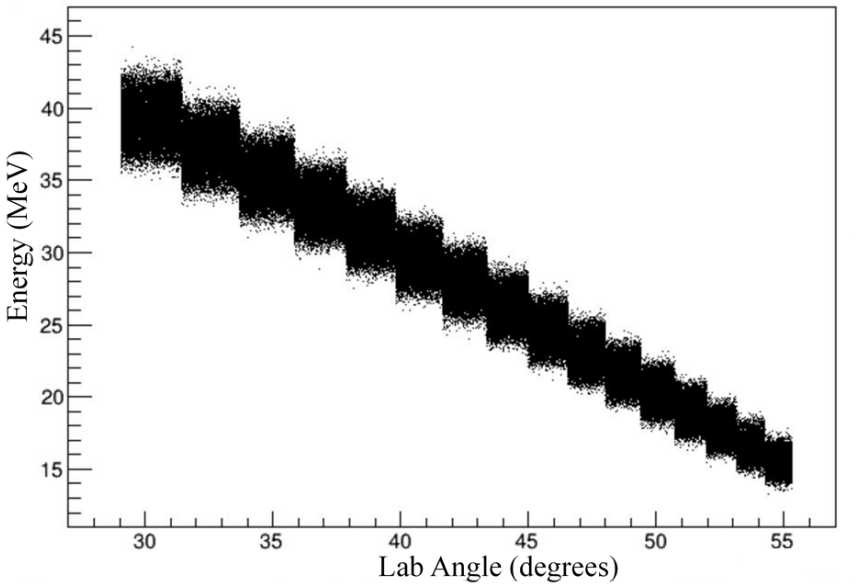

Figure 3.9: Simulation of the ^{93}Kr(d,d)^{93}Kr reaction

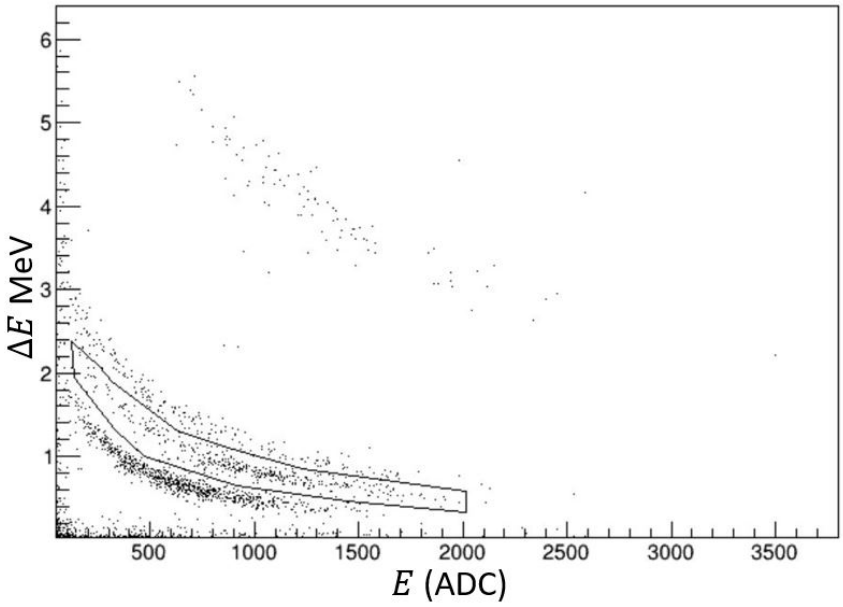

Figure 3.10: Deuteron gate used during CsI(Tl) calibration

proceed with calculating the gain for each sector with equation (3.3). Firstly, the pedestal must be subtracted from the experimental data. Then the data is scaled continuously while the fit is tested with a 2-D Poisson chi-squared test. The scaling

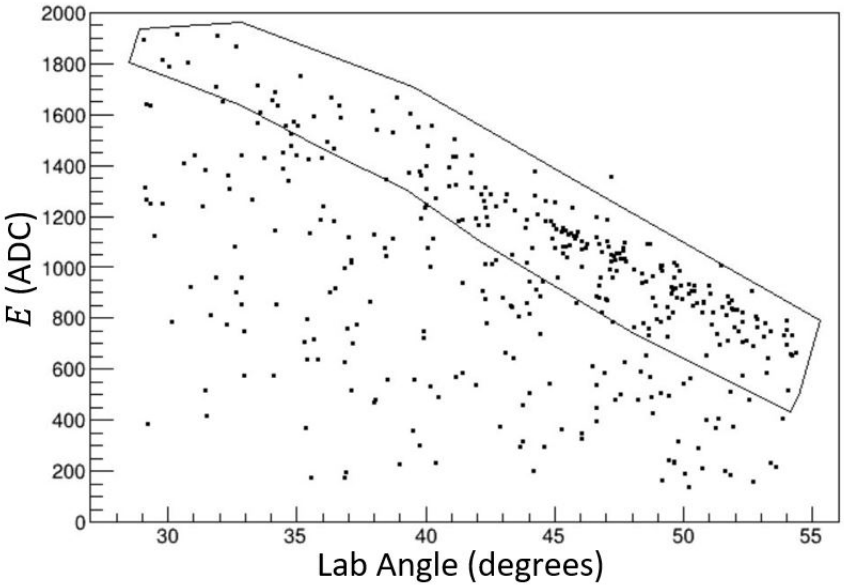

Figure 3.11: Elastic scattering locus cut for CsI(Tl) calibration

factor at which the chi-squared value is minimized, is the gain for the corresponding sector. This process is repeated for the other 15 sectors. With all detector gain values determined, the CsI(Tl) detector was then calibrated.

3.3 Particle Identification

In the introduction to Chapter 3, the idea of reaction channels was briefly mentioned. What this concept refers to is the different allowed reactions for the beam of ^{93}Kr. With the beam impinged on a D_2 target, single nucleon transfers are expected along with scattering reactions. In the case of ^{93}Kr, the reactions of interest are, ^{93}Kr(d,p)^{94}Kr, ^{93}Kr(d,d)^{93}Kr and ^{93}Kr(d,t)^{92}Kr. Since there are three reaction channels, we need to be able to differentiate and isolate them individually for analysis. This is done using the silicon YY1 detector which is coupled to the CsI(Tl) scintillator detector. Most incident light particles will not stop but only lose energy as they pass

throught the YY1 detector which, as explained by equation (3.1), is proportional to charge, therefore allowing for differentiation of light particles by Z. Next, the light particle deposits the total remaining energy into the CsI(Tl) detector which is the remaining kinetic energy. Thus allowing for differentiation by mass.

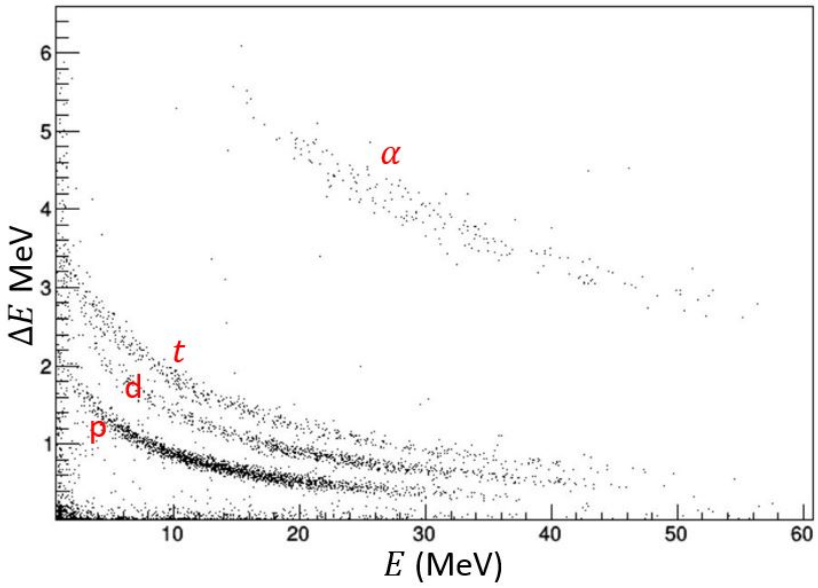

Figure 3.12: Particle identification plot resulting from ^{93}Kr beam impinged on D_2 target

This is shown in Figure 3.12 where the ΔE results from energy loss in the YY1 detector and E results from the remaining energy deposited in the CsI(Tl) detector. The light nuclei from the nuclear reactions are seen as distinct bands which facilitates their identification. The data in this plot is gated on the ^{93}Kr peak within the IC as shown in Figure 3.1 which means the proton (p) result from the reaction ^{93}Kr(d,p)^{94}Kr, the deuterons (d) from the reaction ^{93}Kr(d,d)^{93}Kr and so on. Using this ΔE-E technique, individual reaction channels may be selected for further analysis.

3.4 Excitation Spectra and Angular Distribution of ^{93}Kr

In Figure 3.11 the locus of the ^{93}Kr(d,d)^{93}Kr reaction was identified. This represents the reaction where the ^{93}Kr recoil nucleus remains in the ground state. When the recoil nucleus goes into an unknown excited state, the resulting light particle has a lower energy. This is a key point to the reconstruction of Q-value spectra, a spectrum representing the change in initial and final energy of the kinematic reactions. In the following sections, the method of analysis which is dependent on the identification of the light particle will be presented in Section 3.4.1. Following, this method employed in the analysis of both the ^{93}Kr(d,d)^{93}Kr and ^{93}Kr(d,p)^{94}Kr reaction which will be detailed in Sections 3.4.2 and 3.4.3.

3.4.1 Missing Mass Technique

With the experimental setup used at IRIS, we are reliant on the information given by the ejected light particles to create Q-value spectra. When the identity of the resulting particles change (i.e. ^{93}Kr$\longrightarrow$^{93}Kr*,^{94}Kr,...), we must still be able to resolve the Q-value of the reaction with the mass of the recoil nucleus being unknown. To do so, the missing mass technique is employed.

In general, a reaction takes the form $a + b \rightarrow c + d$ which has Q-value (in natural units, c=1):

$$Q = m_a + m_b - m_c - m_d \tag{3.6}$$

Where m_a, m_b, m_c and m_d are the rest masses of the corresponding particles. If particle d is in an excited state then the rest mass can no longer be used in equation (3.6). Thus, this mass is rewritten as follows:

$$m_d = \sqrt{m_a^2 + m_c^2 - m_b^2 + 2m_b(T_a + m_a) - 2(T_a + m_a + m_b)(T_c + m_c) + P_a P_c \cos\theta_c} \tag{3.7}$$

where T_a, T_c is the kinetic energy of the respected particles and P_a, P_c are the momenta of these particles which are both defined as:

$$P_a = \sqrt{(T_a + m_a)^2 + m_a^2} \tag{3.8}$$

$$P_c = \sqrt{(T_c + m_c)^2 + m_c^2} \tag{3.9}$$

Altogether, the Q-value is generated from the data collected at IRIS with,

$$\begin{aligned} Q &= m_a + m_b - m_c - \\ &\sqrt{m_a^2 + m_c^2 - m_b^2 + 2m_b(T_a + m_a) - 2(T_a + m_a + m_b)(T_c + m_c) + P_a P_c \cos\theta_c} \end{aligned} \tag{3.10}$$

Within this equation, m_a, m_b and m_c are known values while T_a, T_b, P_a, P_b and θ_c are retrieved from the detector data. To then convert to excitation energy, for the ^{93}Kr(d,d)^{93}Kr reaction we have the relation,

$$E_{exc} = -Q \tag{3.11}$$

and for the ^{93}Kr(d,p)^{94}Kr reaction we have the relation,

$$E_{exc} = Q_{g.s.} - Q \tag{3.12}$$

where $Q_{g.s.}$, the ground state Q-value of the ^{93}Kr(d,p)^{94}Kr reaction, is equal to 3.059 MeV.

Given the method above, it will allow for the information on the energy and angle of the light particles gathered within the detectors to be converted to an excitation energy spectrum for the reaction channels of interest, namely, ^{93}Kr(d,d)^{93}Kr and ^{93}Kr(d,p)^{94}Kr. The resulting excitation energy spectra are of importance as they will allow for the excited states of ^{93}Kr and ^{94}Kr to be located and further, give insight into the nuclear structure of these isotopes.

3.4.2 Excitation Energy Spectra of the ^{93}Kr(d,d)^{93}Kr Reaction

Continuing from the information given in the Section 3.4.1, the excitation spectrum is generated with the relation $E_{exc} = -Q$ where the Q-value is given by equation (3.10). Within the ^{93}Kr(d,d)^{93}Kr reaction, there are two types of reactions which are detailed in Section 1.5. The first type of reaction is elastic scattering which will form the ground state peak at 0 MeV while the second type of reaction is inelastic scattering which will generate the excited states of ^{93}Kr.

Shown in Figure 3.13, is the excitation spectrum for the ^{93}Kr(d,d)^{93}Kr reaction integrated over all angles covered by the forward angle YY1-CsI(Tl) detector. Within

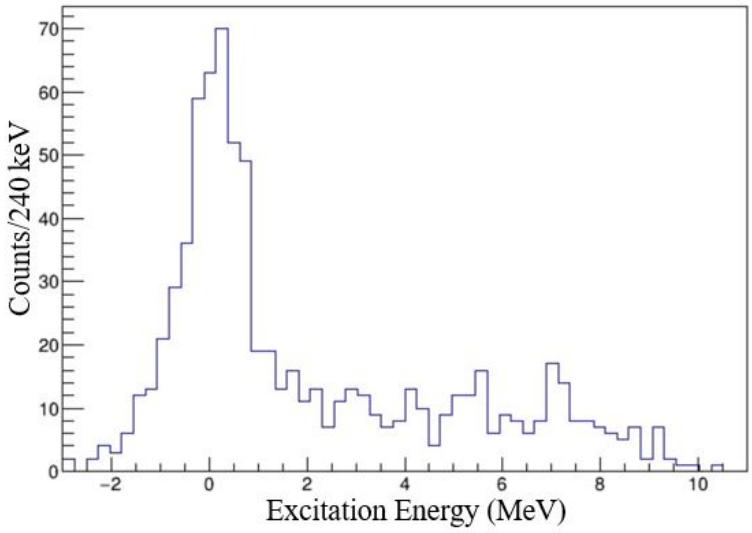

Figure 3.13: Full detector excitation energy of the ^{93}Kr(d,d)^{93}Kr reaction

the figure, a strong peak centered at 0 MeV is formed. For a deeper understanding of this peak and other states, it is important to understand how these states change with angle. Due to low statistics in the forward angle detectors, the data was only grouped into 3 angular regions as shown in Figure 3.14.

Prior to drawing any conclusions on the apparent behaviour of these states, the background must first be quantified and subtracted. But, this only represents part of process in trying to isolate a state as neighbouring states must also be removed. Within the resolution of the measured excitation energy, the large peak at 0 MeV seen in Figure 3.13 may be a convolution of the ground state with further excited states. In Figure 3.14(a) there is insufficient data to draw any conclusions but in Figure 3.14(b) we can see the emergence of two peaks around the 0 MeV region. Further, in Figure 3.14(c) the 0 MeV peak appears to having a skew hinting at contribution from further excited states. The emergence of the two peaks in Figure 3.14(b) gives some insight into the convolution of states around 0 MeV but further analysis is required.

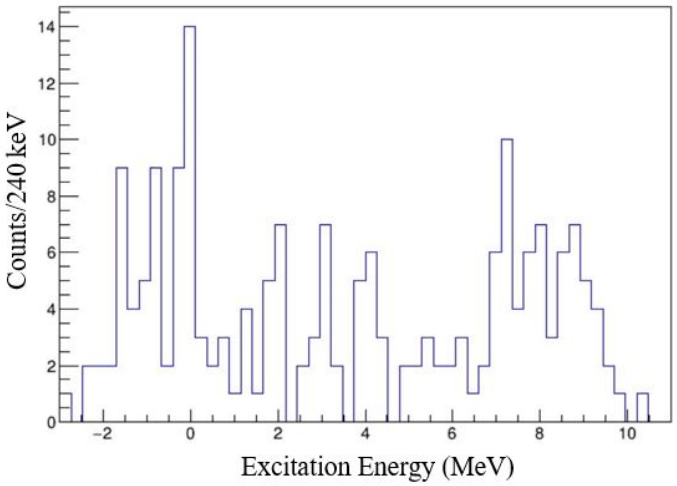

(a) YY1 Rings 0 - 4

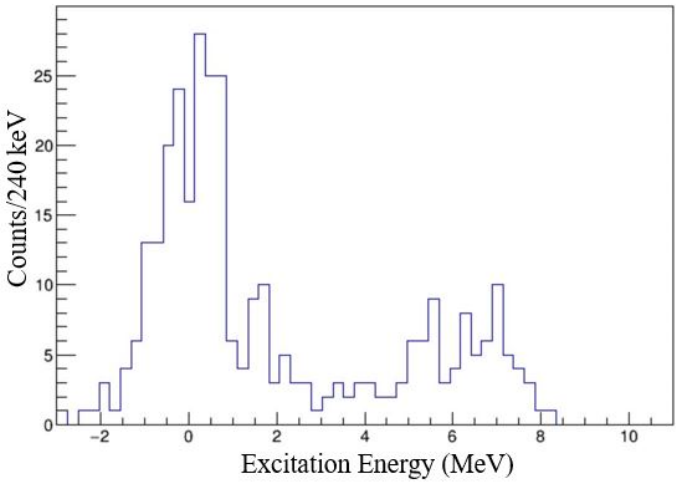

(b) YY1 Rings 5 - 9

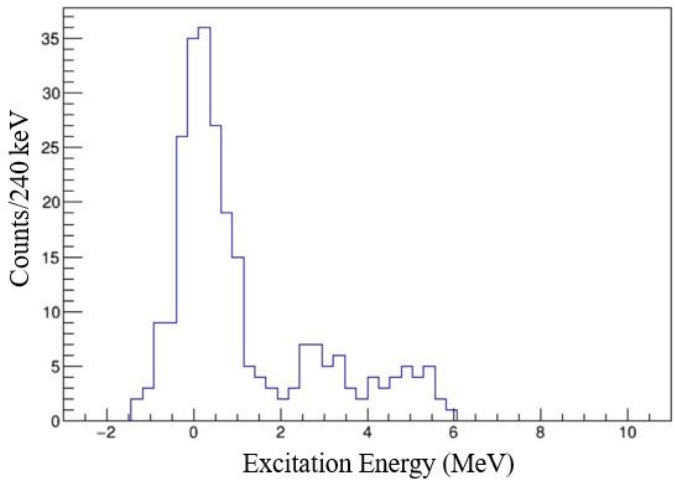

(c) YY1 Rings 10 - 14

Figure 3.14: Excitation energy of the ^{93}Kr(d,d)^{93}Kr reaction in 3 angular regions

3.4.3 Excitation Energy Spectra of the ^{93}Kr(d,p)^{94}Kr Reaction

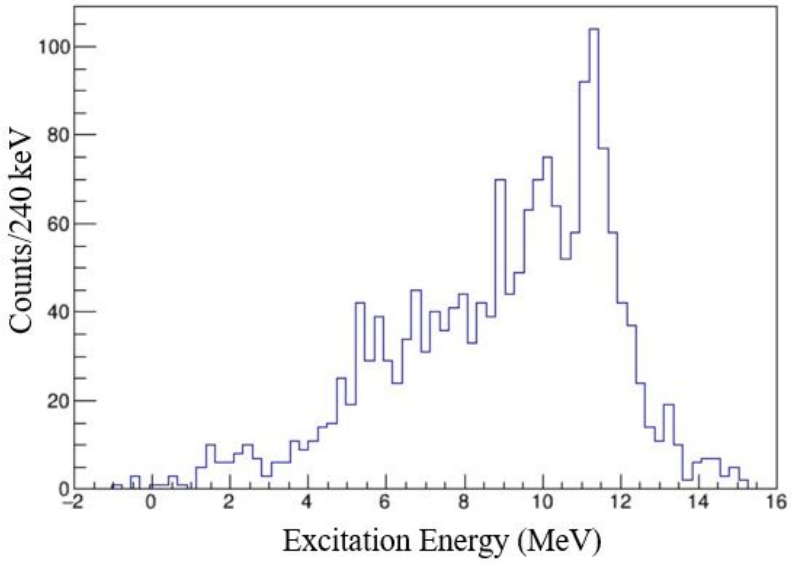

Figure 3.15: Full detector excitation energy of the ^{93}Kr(d,p)^{94}Kr reaction

Similar to the analysis conducted in Section 3.4.2, the data collected during the experiment was used to generate an excitation spectra with the missing mass technique described in Section 3.4.1. Due to the nature of this nuclear reaction, being a transfer reaction (described in Section 1.5), to generate the excitation energy spectrum from a Q-value spectrum we must consider the energy released in the process of the heavy nucleus gaining a neutron from the light nucleus, e.g. the ground state Q-value of the reaction. Therefore, an excitation energy spectrum was generated from the Q-value as $E_{exc} = 3.059 \text{ MeV} - Q$.

The background contribution in the ^{93}Kr(d,p)^{94}Kr reaction results from the Ag foil and N-body phase space. For the Ag foil background contribution, an excitation spectra is generated similarly to that in Figure 3.15 but with the data from runs with

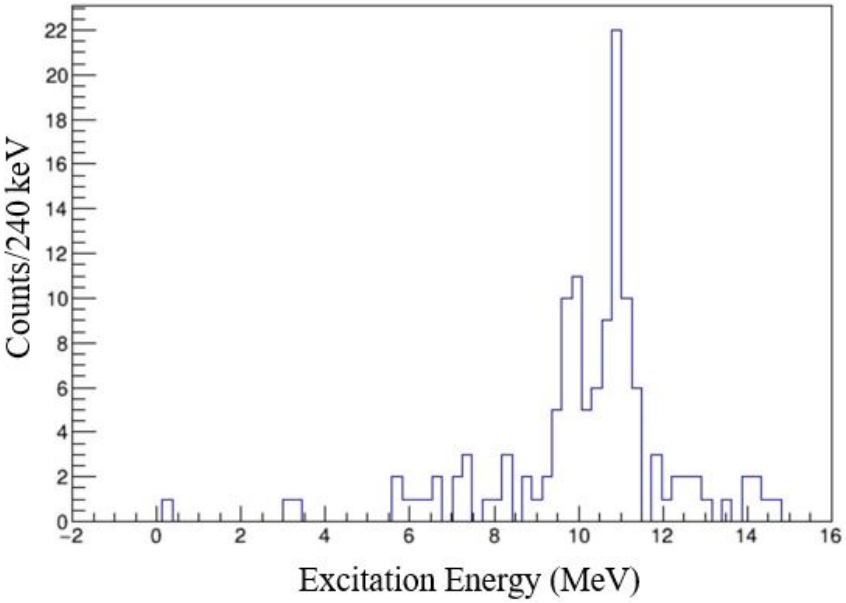

Figure 3.16: Ag foil background for the ^{93}Kr(d,p)^{94}Kr reaction

no D_2 target, resulting in Figure 3.16. Within this figure we see two large peaks form at approximately 9.5 MeV and 11 MeV. These peaks are also clearly seen in the angle integrated spectrum shown in Figure 3.15. The N-body phase space contribution is a result of a reaction of the form,

$$A + b \longrightarrow c_1 + c_2 + ... + c_{N-1} + D \tag{3.13}$$

where the heavy particle A and light particle b break up into N-1 light particles and a heavy recoil nucleus. The background contribution from such a reaction would be more dominant in the higher energy region of the excitation energy spectrum. Therefore, both sources of background considered together, the contributions from the Ag foil and N-body phase space are largely in the higher energy portion of the excitation energy spectrum. From this we can assume the background to be negligible

in the region $E_{exc} < 3$ MeV.

Shown in Figure 3.17 is the ^{93}Kr(d,p)^{94}Kr reaction excitation spectrum subdivided into 3 angular regions. No background is overlayed due to it being presumed as negligible in the region of interest. The emergence of two peaks can be seen within this region (0 - 3 MeV). Fitting both with Gaussians as seen in Figure 3.18, the first has an energy of 1.5±0.3 MeV and the second has an energy of 2.3±0.3 MeV. These energy values agree with those found in the backward angle detectors. Within Figure 3.17, we see both states are at a maximum in the first angular region while their counts and resolution are reduced in the second and third angular region.

Currently only two excited states in ^{94}Kr have been determined, a 2^+ state at 665.5 keV and (4^+) state at 1.518 MeV. Both excited states were determined by Ref.[14] with γ-ray spectroscopy of the spontaneous fission products of ^{248}Cm. In Ref.[5], the theoretically determined excited states near the two peaks found in Figure 3.18 include 2^+ and 4^+ states near 1.3 MeV as well as 4^+ and 6^+ states near 2.4 MeV. In Ref.[6], a 4^+ state is expected near 1.5 MeV as well.

From Ref.[5][6][14] it would be expected that the peak observed in Figure 3.18 at 1.5±0.3 MeV is a 4^+ state. That being said, further analysis is required to properly understand the distribution of both peaks which in turn would generate a cross section. From here, spin and parity could properly be assigned to the suspected energy levels.

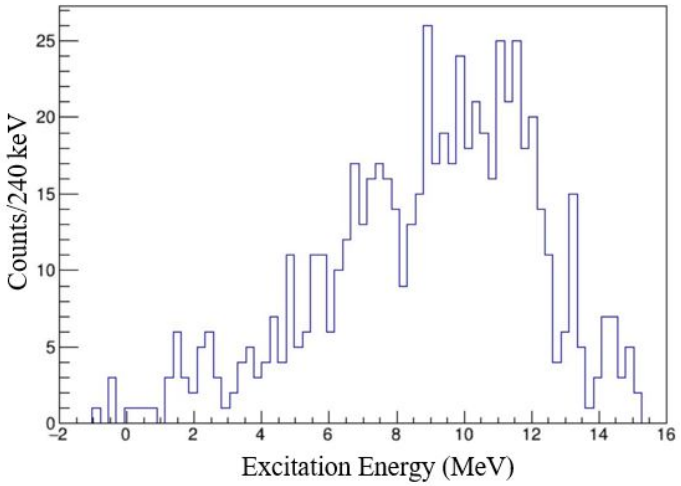

(a) YY1 Rings 0 - 4

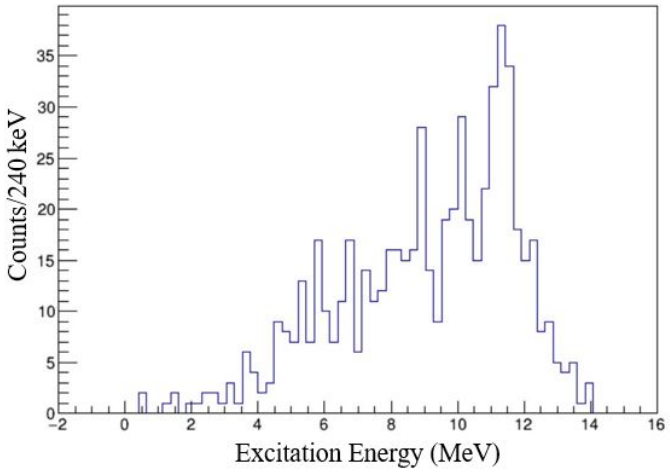

(b) YY1 Rings 5 - 9

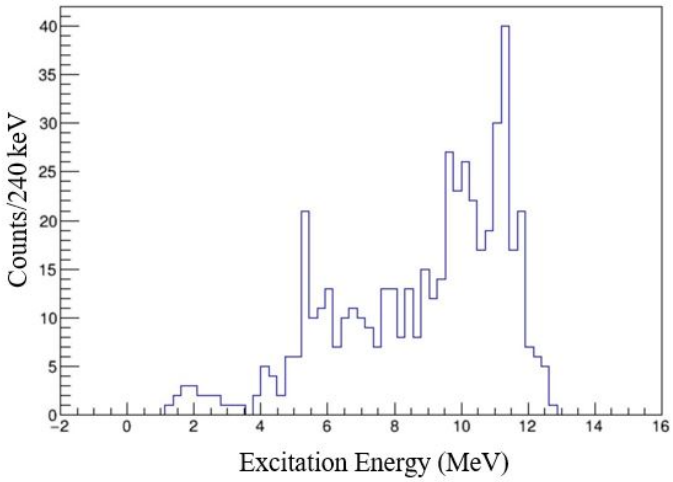

(c) YY1 Rings 10 - 14

Figure 3.17: Excitation energy of the ^{93}Kr(d,p)^{94}Kr reaction in 3 angular regions

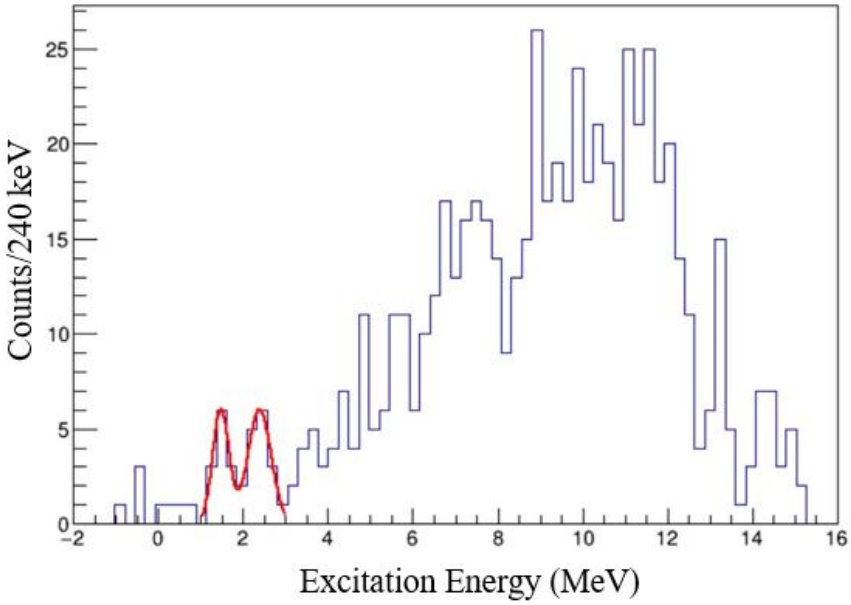

Figure 3.18: Fitted excited states in YY1 rings 0-4 of reaction ^{93}Kr(d,p)^{94}Kr

Chapter 4

Conclusion

The nuclear properties of ^{93}Kr and ^{94}Kr were explored at IRIS through scattering reactions and single neutron transfer reactions. For both, an excitation spectrum was created. In the excitation spectrum of ^{93}Kr, identification of single state peaks was rendered difficult by the limited resolution. In the excitation spectrum of ^{94}Kr, two peaks were identified at 1.5±0.3 MeV and 2.3±0.3 MeV. This agreed with findings in the backward angle detector for the ^{93}Kr(d,p)^{94}Kr reaction. Further analysis is required to assign spin and parity to these states as well as understanding their angular distribution.

There are many sources which may have contributed to the low resolution of the data. The suspected primary source of uncertainty was the inability to properly identify the target thickness which was discussed in Section 3.2.2. This was due to the fact that both the beam energy and the detector gain were varying. Another suspected source of uncertainty results from the low beam statistics which largely impacted the calibration of the CsI(Tl) detector.

Although the question as to whether shell evolution is present in neutron-rich krypton nuclei remains open, it continues to be under investigation.

Bibliography

[1] Kenneth S Krane. *Introductory Nuclear Physics*. Wiley, New York, NY, 1988.

[2] *Nuclear Power*. Nuclear shell model. https://www.nuclear-power.net/nuclear-power/reactor-physics/atomic-nuclear-physics/atom-properties-of-atoms/atomic-nucleus/nuclear-shell-model/.

[3] Maria Goeppert Mayer. On closed shells in nuclei. ii. *Physical Review*, 75:1969–1970, 1949.

[4] R. Kanungo. IRIS EEC Submission, June 2017.

[5] Tomás R. Rodríguez. Structure of krypton isotopes calculated with symmetry-conserving configuration-mixing methods. *Phys. Rev. C*, 90:034306, Sep 2014.

[6] M. Albers et al. Evidence for a smooth onset of deformation in the neutron-rich kr isotopes. *Phys. Rev. Lett.*, 108:062701, 2012.

[7] Bohr and Kalckar. *Mater. Fys. Med. Dan. Vid. Selsk.*, 14, 1937.

[8] Kris Heyde. *Basic Ideas and Concepts in Nuclear Physics*. Institute of Physics, 2004.

[9] H. Morinaga. Interpretation of some of the excited states of $4n$ self-conjugate nuclei. *Phys. Rev.*, 101:254–258, Jan 1956.

[10] Kris Heyde and John L. Wood. Shape coexistence in atomic nuclei. *Rev. Mod. Phys.*, 83:1467–1521, Nov 2011.

[11] R. Kanungo. Iris: The isac charged particle reaction spectroscopy facility for reaccelerated high-energy isol beams. *Hyperfine Interac.*, 225:235–240, 2014.

[12] Jaspreet Randhawa. *Investigations on states of ^{20}Mg and spallation reaction effects for constraining nuclear physics inputs for X-ray bursts*. PhD thesis, Saint Mary's University, 2017.

[13] *Micron Semiconductor Ltd.* YY1. http://www.micronsemiconductor.co.uk/product/yy1/.

[14] T. Rzaca-Urban et al. Shapes of the neutron-rich $^{88-94}$kr nuclei. *Eur Phy J A*, 9:165–169, 2000.